ACS APPLIED MATERIALS & INTERFACES

www.acsami.org Research Article

The Dual Role of Bridging Phenylene in an Extended Bipyridine System for High-Voltage and Stable Two-Electron Storage in Redox Flow Batteries

Mingguang Pan, Yan Lu, Shuyu Lu, Bo Yu, Jie Wei, Yuzhu Liu, and Zhong Jin*

Cite This: https://doi.org/10.1021/acsami.1c09019 Read Online

ACCESS | Metrics & More | Article Recommendations | SI Supporting Information

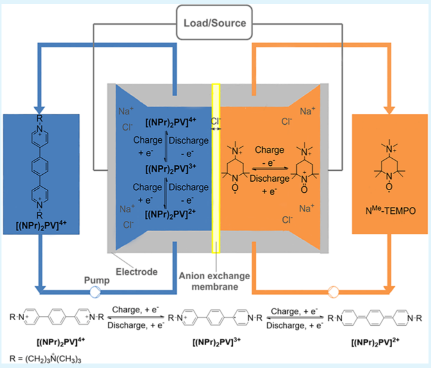

ABSTRACT: Aqueous organic redox flow batteries (AORFBs) are regarded as a promising solution for grid-scale and sustainable energy storage, but some long-standing problems such as low energy density and cycling stability should be resolved. Herein, a highly soluble bipyridine modified with a bridging phenylene group and two quaternary ammonium terminals, namely, **$[(NPr)_2PV]\cdot 4Cl$**, was synthesized and used as an ultralow-potential and two-electron storage anolyte for AORFBs. The phenylene group, which is linked but not coplanar with the two pyridinium redox centers, can thus prevent their communication and result in an exceptionally low redox potential (−0.77 V vs standard hydrogen electrode, 2e$^-$). Moreover, the introduction of a phenylene group can warrant a certain degree of large *π*-conjugation effects and mitigate the intramolecular Coulombic repulsion between the two positively charged pyridinium centers, thus helping to enhance the electrochemical stability. When paired with 4-trimethylammonium-TEMPO as the catholyte, **$[(NPr)_2PV]\cdot 4Cl$** enabled an exceptionally high cell voltage up to 1.71 V. The AORFB delivers outstanding battery performances, specifically, ~89% energy efficiency, ~100% Coulombic efficiency, and ~99.94% capacity retention per cycle during a long-term cycling process. The two overlapped single-electron reductions of **$[(NPr)_2PV]\cdot 4Cl$** from the initial cationic form to the monoradical form and then to the quinoid form during the charging process were clearly verified by a series of spectroscopic techniques, including no-deuterium nuclear magnetic resonance and electron paramagnetic resonance. This work presents a significant improvement for the construction of high-voltage AORFBs by virtue of the designability, diversity, and tunability of multiredox organic molecules.

KEYWORDS: *high voltage, two single-electron reductions, aqueous organic redox flow batteries, extended bipyridine, pH-neutral*

1. INTRODUCTION

Driven by the increasing concerns on the environmental crisis, our society is in a booming demand on clean energy sources such as solar and wind power.[1] However, the output intermittency and fluctuation of renewable energy impede their direct supply into power grids.[2] Therefore, it is highly desired to develop reliable and sustainable large-scale energy storage techniques. Redox flow batteries (RFBs) have been recognized as a promising technology for grid-scale electricity storage (up to MW/(MW h)).[3] The ingenious configuration of RFBs endows numerous advantages in comparison with traditional static cells, including decoupled energy and power, high current and power capability, excellent scalability, and safe operation.[4] Among existing RFB systems, aqueous organic redox flow batteries (AORFBs), where energy is stored and outputted via the reversible redox reactions of water-soluble organic active molecules, hold great promise for "green" electrochemical energy storage.[5−13] Compared with inorganic species, redox-active organic materials are advantageous due to their extensive structural diversity, tunable electrochemical properties, high natural abundance, and potentially low costs.[14−19] However, the energy density of AORFBs is greatly limited by the aqueous solubility and redox potential range of organic active species.[7−45] In recent years, methyl viologen and its derivatives have gained popularity as anolytes in pH-neutral aqueous conditions. However, the effective redox potential of methyl viologen is −0.45 V vs standard hydrogen electrode (SHE), and its second electron reduction is irreversible, which restrict its practical application. Normally, the redox potential of viologen derivatives, such as 1,1′-bis[3-(trimethylammonio)propyl]-4,4′-bipyridinium tetrachloride,[21,23] is located around −0.54 V vs SHE (−0.35 and −0.72 V for the first and second electron reductions, respectively). Liu et al. reported the first *π*-conjugation-

Received: May 15, 2021

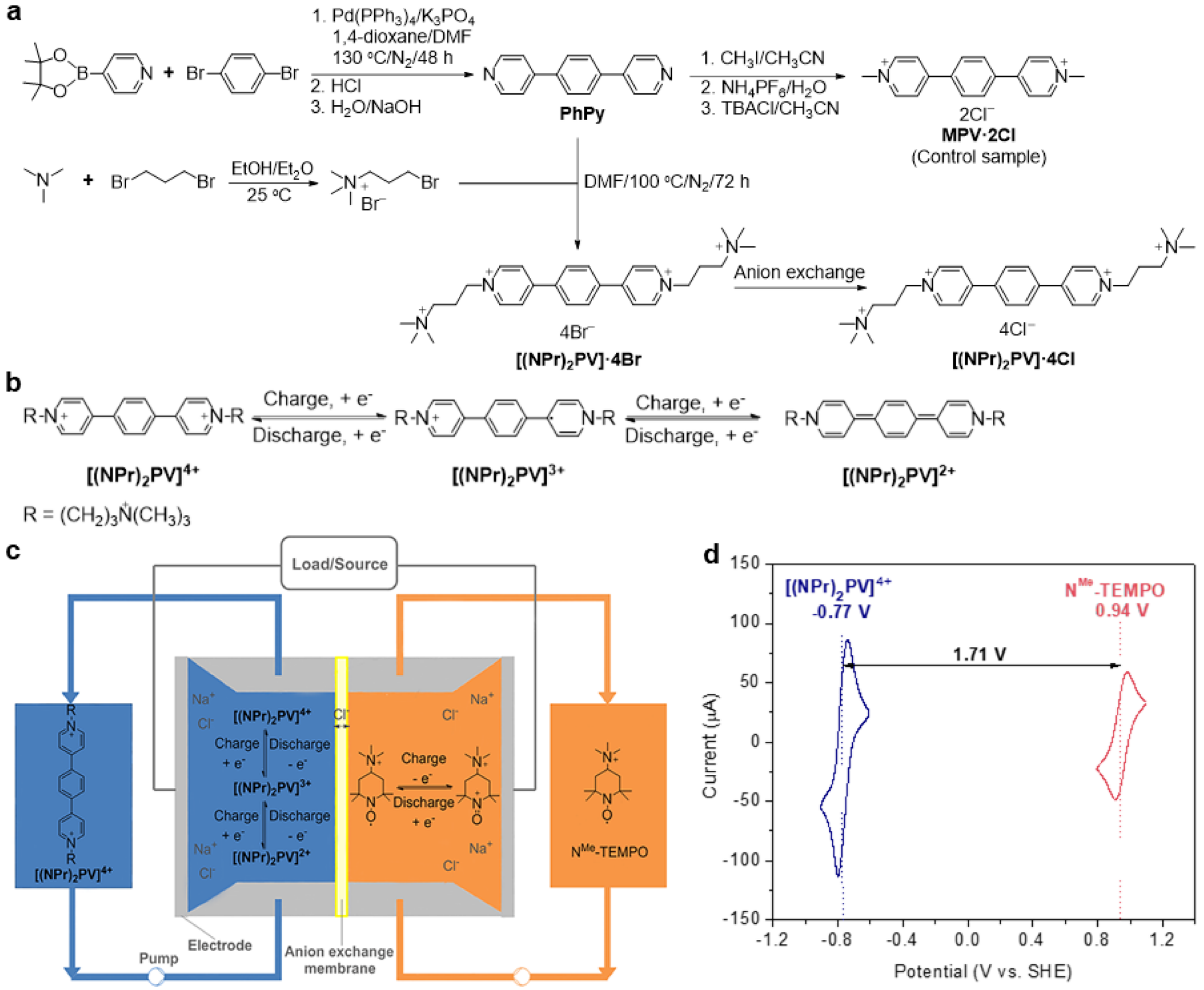

Figure 1. Synthesis and working mechanism of extended bipyridines. (a) Synthetic routes of [**(NPr)$_2$PV**]**·4Cl** and **MPV·2Cl** (control sample). (b) Plausible reversible redox reaction pathways of the [**(NPr)$_2$PV**]**·4Cl** analyte during the charge−discharge process of AORFBs. (c) Schematic configuration of the [**(NPr)$_2$PV**]**·4Cl**/N^{Me}-TEMPO AORFB and its anodic and cathodic half-cell reactions. (d) CV curves of 4 mM [**(NPr)$_2$PV**]**·4Cl** and 4 mM N^{Me}-TEMPO in a 0.5 M NaCl solution.

extended viologen system based on 4,4′-(thiazolo[5,4-d]-thiazole-2,5-diyl)bis(1-(3-(trimethylammonio)propyl)pyridin-1-ium) tetrachloride as a two-electron storage analyte for aqueous organic redox flow batteries, whose redox potential (−0.44 V vs SHE) was only comparable to that of methyl viologen.[22] There is still tremendous room to improve the potential window of viologen analogues. The rational molecular engineering of organic redox-active species with extremely low redox potential, high solubility, and high electrochemical reversibility/stability is highly desirable.

2. RESULTS AND DISCUSSION

Herein, we report the design and synthesis of a π-conjugation-extended and quaternary ammonium-terminated bipyridine, namely, 4,4′-(1,4-phenylene)bis(1-(3-(trimethylammonio)-propyl)pyridin-1-ium) tetrachloride ([**(NPr)$_2$PV**]**·4Cl**) (Figure 1a), which can serve as an analyte with an exceptionally low redox potential (−0.77 V vs SHE, 2e$^-$) in pH-neutral aqueous solution. In this viologen derivative, the two pyridinium moieties are linked by a central phenylene group and grafted with two alkyl quaternary ammonium cation groups, realizing an overlapped two-electron storage behavior accompanied with an ultralow redox potential and high aqueous solubility for AORFBs. The introduction of a bridging phenylene group plays an important role in preventing communication between the two pyridinium redox centers owing to the noncoplanar links between these aromatic rings, thereby resulting in an extremely low redox potential in pH-neutral aqueous environments. Meanwhile, the π-conjugation-extended molecular skeleton helps to enhance the electrochemical stability of the reduced species, originating from the broader electron delocalization and the formation of a quinoid form after the two single-electron reductions (Figure 1b). Additionally, the grafted ammonium cation terminals can improve the aqueous solubility (especially in the reduced state) and greatly increase the intermolecular Coulombic repulsion, thus avoiding dimerization degradation and enhancing the redox reversibility.[32,46] When paired with a high redox potential catholyte, 4-ammonium-TEMPO (N^{Me}-TEMPO), a pH-neutral [**(NPr)$_2$PV**]**·4Cl**/N^{Me}-TEMPO AORFB can be

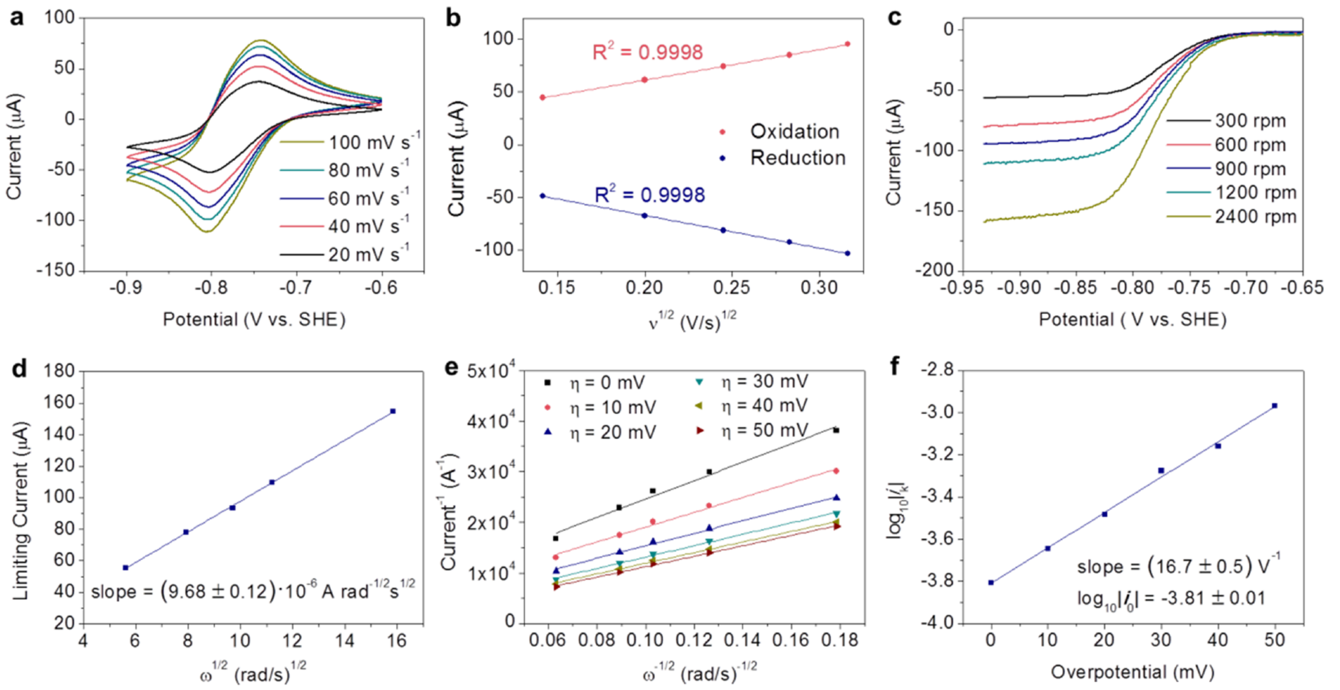

Figure 2. Electrochemical characterizations of **[(NPr)$_2$PV]·4Cl**. (a) CV curves of 4.0 mM **[(NPr)$_2$PV]·4Cl** in a 0.5 M NaCl aqueous solution at the scan rates (ν) between 20 and 100 mV s^{-1}. (b) Plots of the peak current vs $\nu^{1/2}$. (c) LSV curves of 1.0 mM **[(NPr)$_2$PV]·4Cl** in a 0.5 M NaCl solution with a scan rate of 5 mV s^{-1} at different rotation speeds from 300 to 2400 rpm. (d) Levich plot of the limiting current vs the square root of the rotation rate. (e) Koutecký–Levich plot at different reduction overpotentials η, yielding the mass transfer-independent current i_k (as $\omega^{-1/2} \to 0$, $i_k = i$). (f) Tafel plot of log$_{10}|i_k|$ vs overpotentials η, yielding the rate constant (k_0) and the transfer coefficient (α).

constructed (Figure 1c), enabling an ultrahigh open-circuit voltage of 1.71 V (Figure 1d) and a considerable theoretical energy density up to 63.6 W h L^{-1} for the full battery. Benefitting from the outstanding reversibility of this redox pair, the AORFB maintains ultrahigh energy efficiency (∼89%) and Coulombic efficiency (∼100%) during hundreds of charge–discharge cycles with a high capacity retention of 99.94% per cycle.

The π-conjugation-extended bipyridine skeleton, 1,4-di(pyridin-4-yl)benzene (**PhPy**), was synthesized by a single-step Suzuki–Miyaura reaction of 4-pyridineboronic acid pinacol ester and 1,4-dibromobenzene with a high yield of 90% (Figures S1 and S2), which can be easily scaled up and applied to the synthesis of various extended bipyridine skeletons.[47,48] Then, **PhPy** was reacted with (3-bromopropyl)-trimethylammonium bromide to yield 4,4′-(1,4-phenylene)-bis(1-(3-(trimethylammonio)propyl)pyridin-1-ium) tetrabromide (**[(NPr)$_2$PV]·4Br**) without the need of further purification through resource-intensive chromatography. Subsequently, an anion exchange process was conducted by using an Amberlite IRA-900 chloride form resin to quantitatively convert **[(NPr)$_2$PV]·4Br** to the chloride form, **[(NPr)$_2$PV]·4Cl**, thereby eliminating the interference of redox-active bromide in the battery tests (Figures S3 and S4). The whole synthesis route achieved high overall yield and purity, allowing large-scale production. As a control sample, phenylene-bridged methyl viologen dichloride (**MPV·2Cl**) was also synthesized from the *N*-methylation of **PhPy** by using CH_3I, following two steps of anion exchange, i.e., NH_4PF_6/H_2O and ^{n}Bu$_4$NCl/CH_3CN, respectively (Figures S5 and S6). **MPV·2Cl** exhibited high solubility both in deionized water (2.20 M) and NaCl solution (2.09 M) (Figure S7), on account of the nonplanar **PhPy** skeleton that could impede π–π interaction-induced intermolecular aggregation. The cyclic voltammetry (CV) profiles of **MPV·2Cl** present a relatively low redox potential at −0.70 V vs SHE; however, the redox reversibility of **MPV·2Cl** is not satisfactory (Figure S8a), which is similar to the second redox couple of methyl viologen (MV^{+}/MV^{0}) that suffers severe side reactions due to the formation of an insoluble, charge-neutral MV^0 state in aqueous solution.[49]

The highly cationized **[(NPr)$_2$PV]$^{4+}$** species exhibited high solubility in deionized water (1.29 M) and 2.0 M NaCl solution (1.18 M) (Figure S9). The CV of **[(NPr)$_2$PV]·4Cl** displayed only one broad reversible redox couple at −0.77 V vs SHE, attributing to the completely overlapped two single-electron reductions (Figure 2a).[47,50] To the best of our knowledge, this redox potential is among the lowest records of the reduction potentials for two-electron storage anolytes that have been experimentally determined in pH-neutral aqueous electrolytes.[15] At different scan rates, both the oxidation and reduction peak currents of the redox couple of **[(NPr)$_2$PV]$^{4+}$** had a linear relationship with the square root of the scan rate ($\nu^{1/2}$), indicating a reversible and diffusion-controlled redox process (Figure 2b). Moreover, as revealed by the CV curves between the 1st and 100th cycles (Figure S8b), **[(NPr)$_2$PV]·4Cl** displayed excellent reversibility, making it suitable for the establishment of stable high-voltage AORFBs.

The electrochemical kinetic properties of **[(NPr)$_2$PV]·4Cl**, including the diffusion coefficient (D) and the kinetic rate constant (k_0), were studied by using linear sweep voltammetry (LSV) on a glassy carbon rotating disk electrode (Figure 2c–f). The LSV scans were conducted at a rate of 5 mV s^{-1} from −0.65 to −0.93 V vs SHE (Figure 2c). The linear Levich plot was constructed for the two single-electron reductions of **[(NPr)$_2$PV]$^{4+}$** using the limiting current (i) and the square root of the rotation speed ($\omega^{1/2}$) to obtain a D value of 2.58(4)

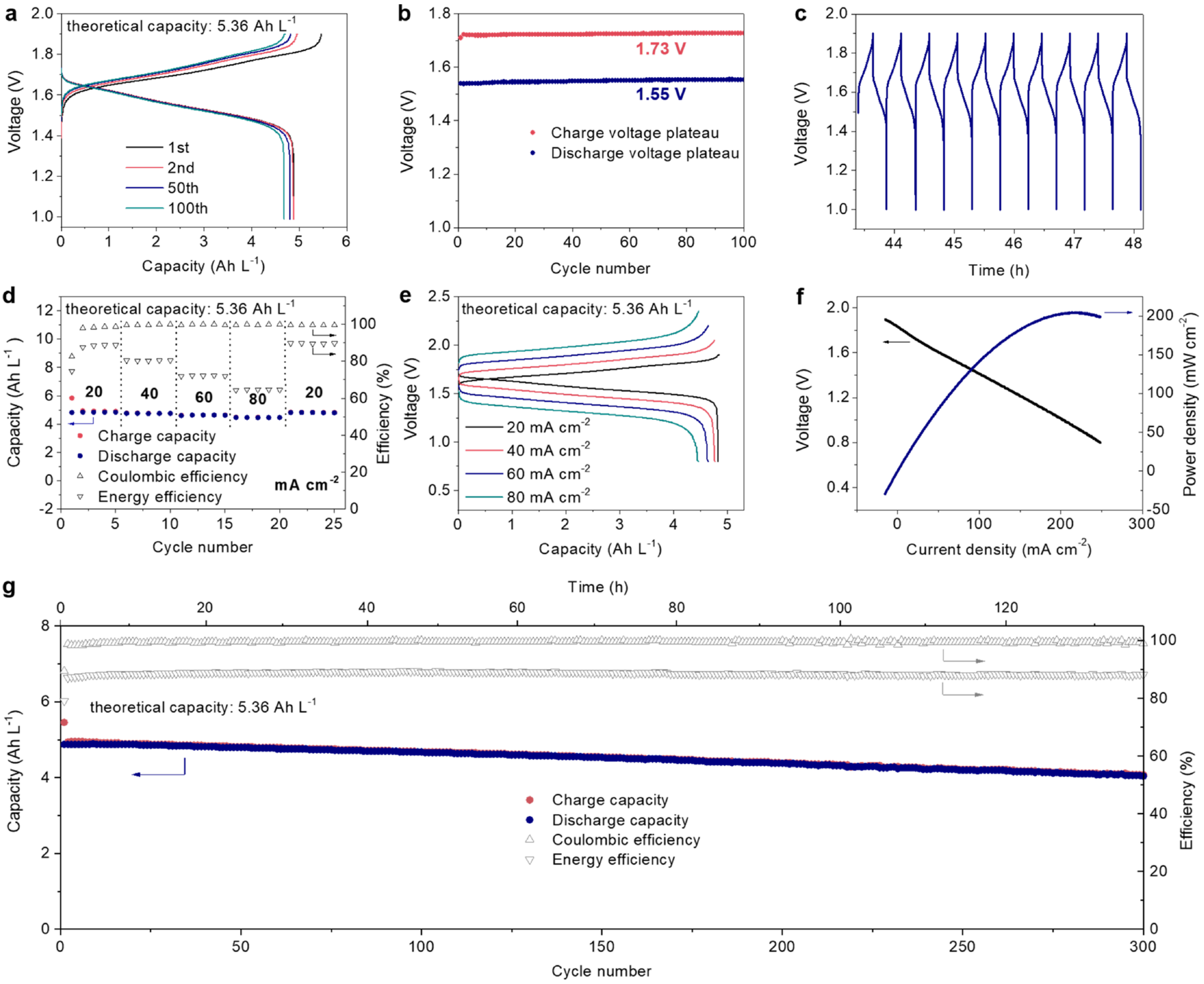

Figure 3. Battery performances. (a) Typical galvanostatic charge−discharge profiles of the [**(NPr)$_2$PV**]**·4Cl**/N^{Me}-TEMPO AORFB at 20 mA cm^{-2}. (b) Charge and discharge voltage plateaus per cycle during 100 charge−discharge cycles. (c) Representative voltage vs time curves recorded between the 91st and 100th cycles. (d) Rate performance measured between the current densities from 20 to 80 mA cm^{-2}, showing the charge capacity, discharge capacity, Coulombic efficiency, and energy efficiency vs cycle number. (e) Representative charge−discharge curves of the AORFB at different current densities. (f) *I*−*V* polarization and power density of the AORFB at an ∼100% state of charge. (g) Cycling performance showing the charge capacity, discharge capacity, Coulombic efficiency, and energy efficiency vs cycle number. Conditions: anolyte, 0.1 M [**(NPr)$_2$PV**]**·4Cl** in 2.0 M NaCl solution; catholyte, 0.2 M N^{Me}-TEMPO in 2.0 M NaCl solution; current density, 20 mA cm^{-2}.

× 10^{-6} cm^2 s^{-1} for [**(NPr)$_2$PV**]$^{4+}$ (Figure 2d). According to the Koutecký−Levich equation and the Tafel plot, the rate constant (k_0) and the charge transfer coefficient (α) of [**(NPr)$_2$PV**]$^{4+}$ were calculated to be (4.09 ± 0.09) × 10^{-3} cm s^{-1} and 0.49 ± 0.02, respectively. The k_0 value of [**(NPr)$_2$PV**]$^{4+}$ was nearly 15 times that of MV, confirming its fast electron transfer kinetics.[13]

A flow battery was constructed using 0.1 M [**(NPr)$_2$PV**]**·4Cl** and 0.2 M N^{Me}-TEMPO in a 2.0 M NaCl supporting electrolyte for the anolyte and catholyte, respectively; additionally, a Selemion AMV anion-exchange membrane was used as the separator for Cl$^-$ exchange (Figure 1c and Figure S10). In the pH-neutral aqueous solution, [**(NPr)$_2$PV**]**·4Cl** presented two overlapped single-electron reductions, showing one broad reversible redox couple at −0.77 V vs SHE, and N^{Me}-TEMPO underwent a single-electron oxidation at 0.94 V vs SHE, giving rise to a remarkably high cell voltage of 1.71 V (Figure 1d). As a result, a theoretical energy density of 63.6 W h L^{-1} could be envisioned, providing the foundation for constructing high-energy pH-neutral AORFBs.

The charge−discharge performance of the [**(NPr)$_2$PV**]**·4Cl**/N^{Me}-TEMPO AORFBs was measured by adding an excess N^{Me}-TEMPO catholyte to guarantee the complete redox reaction of the [**(NPr)$_2$PV**]**·4Cl** anolyte during cycling. The galvanostatic charge−discharge profiles revealed the high voltage and good stability of the AORFBs (Figure 3). Notably, the assembled AORFBs were high-voltage-tolerant and were able to work well at a cutoff charging voltage of 1.9 V (Figure 3a). During the first charge−discharge cycle, the Coulombic efficiency was 89% due to the consumption of the remaining O$_2$ in the aqueous electrolyte and the reservoir.[29] After the first cycle, the Coulombic efficiency rapidly stabilized as high as ∼100%, demonstrating the negligible side reaction from electrochemical water splitting. This is because the overpotentials of the O$_2$ evolution reaction (OER) and the H$_2$ evolution reaction (HER) on a carbon electrode are very high,

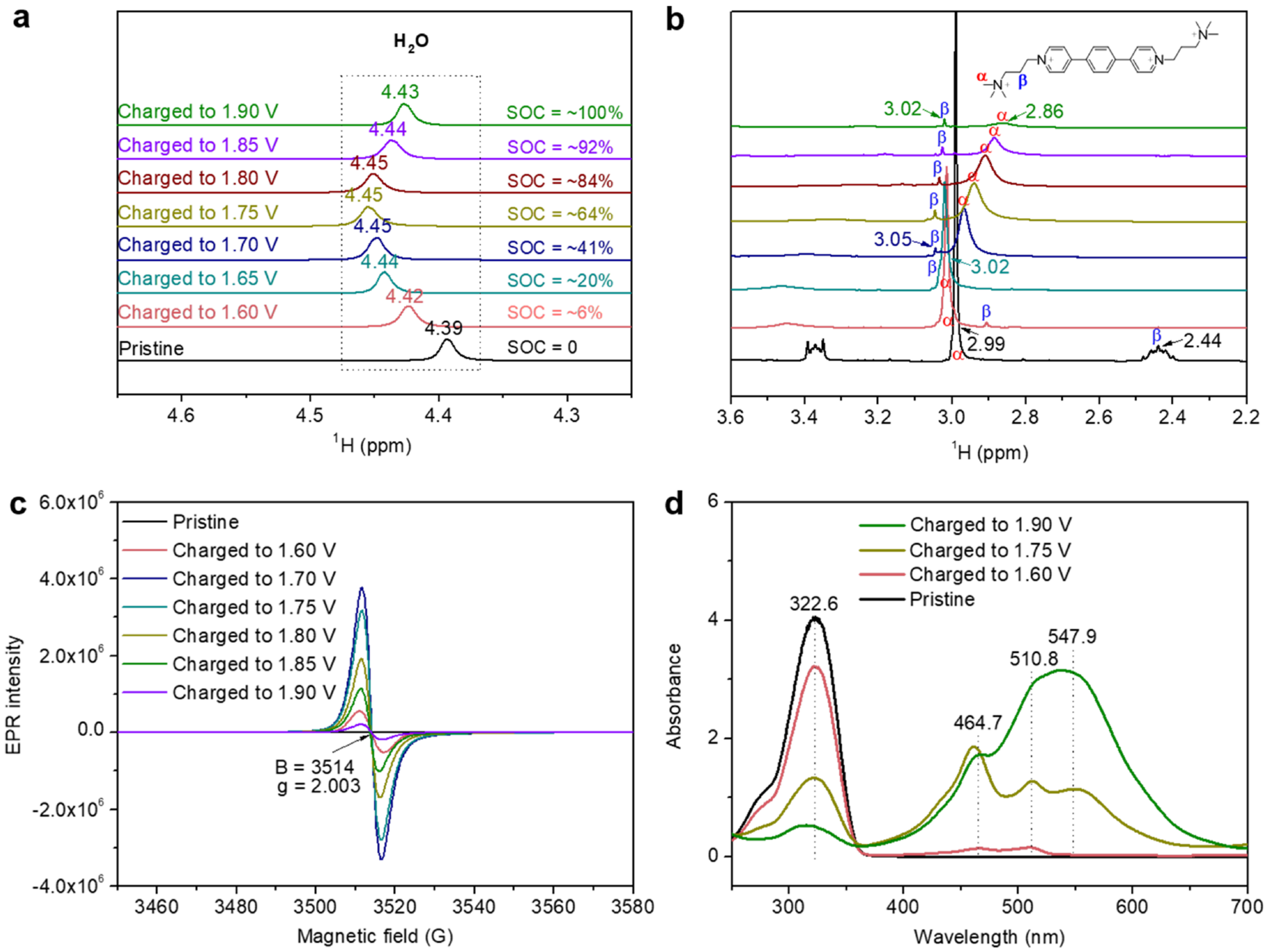

Figure 4. Spectroscopic analyses of the redox mechanism. (a) Partial no-deuterium NMR spectra of water peaks in the 0.1 M [**(NPr)$_2$PV**]**·4Cl** anolyte at different charge states. The ratio of [**(NPr)$_2$PV**]**·4Cl** in the reduced state is referred to as the state of the charge (SOC). (b) Partial no-deuterium NMR spectra of [**(NPr)$_2$PV**]**·4Cl** at different charge states. (c) EPR responses of the 0.1 M [**(NPr)$_2$PV**]**·4Cl** anolyte at different charge states. (d) UV−vis absorption spectra of the 1.0 mM [**(NPr)$_2$PV**]**·4Cl** anolyte at different charge states with a light path length of 1.0 mm through the sample.

which significantly broadens the potential window of water splitting from 1.23 to 2.5 V.[31] In the first discharge step, the AORFB with the 0.1 M [**(NPr)$_2$PV**]**·4Cl** anolyte delivered a capacity of 4.88 A h L^{-1}, which was 91% of the theoretical capacity limit for two-electron storage (5.36 A h L^{-1}). Importantly, the charge and discharge voltage plateaus of the AORFB at a current density of 20 mA cm^{-2} were well maintained at 1.73 and 1.55 V after 100 cycles (~48 h), respectively (Figure 3b,c), demonstrating the high operation voltage and favorable electrochemical stability.

Moreover, the AORFB exhibited an excellent rate capability at current densities ranging from 20 to 80 mA cm^{-2} (Figure 3d,e). The discharge capacity at 80 mA cm^{-2} is 4.46 A h L^{-1}, providing an ~92.5% capacity retention relative to the value at 20 mA cm^{-2}. The maximum power density of the AORFB with 0.1 M [**(NPr)$_2$PV**]**·4Cl** at an ~100% state of charge reached 204 mW cm^{-2} with a corresponding current density of 215 mA cm^{-2} (Figure 3f). The long-term cycling performance of the AORFB was evaluated at 20 mA cm^{-2} for 300 cycles. As shown in Figure 3g, the AORFB exhibited high cycling stability with a total capacity fade of 17.2% after 300 cycles, corresponding to a capacity fade rate of 0.06% per cycle and a time-dependent fade rate of 3% per day. During the long-term cycling process, the AORFB maintained an ultrahigh energy efficiency of ~89% and a Coulombic efficiency of ~100%. Furthermore, when the concentrations of electrolytes were increased to 0.5 M for the [**(NPr)$_2$PV**]**·4Cl** anolyte and 1.0 M for the N^{Me}-TEMPO catholyte, the AORFB still delivered a high volumetric capacity of 18.5 A h L^{-1}, accompanied with a capacity retention of 99.88% per cycle, a Coulombic efficiency of ~100%, and an energy efficiency of 87% (Figures S11 and S12).

To evaluate the electrochemical stability of [**(NPr)$_2$PV**]**·4Cl**, the AORFB was cycled galvanostatically at 20 mA/cm^2 between 1.9 and 1.0 V with a potentiostatic hold after each half-cycle ends until the magnitude of the current density fell below 2 mA/cm^2 (Figure S13). In this case, the AORFB delivered a capacity fade rate of ~0.14% per cycle (7.58% per day), an average energy efficiency of ~89%, and an average Coulombic efficiency of ~100% over 300 cycles. To understand the underlying reason for the capacity degradation, ^{1}H NMR spectra of the catholyte and the anolyte before and after long-term cycling for a time duration of ~6 days were collected (Figures S14 and S15). As revealed by ^{1}H NMR data, the capacity fade should be primarily caused by the crossover and decomposition of N^{Me}-TEMPO. Moreover, as revealed by the CV curves, a new irreversible oxidation peak at 0.99 V vs SHE

https://doi.org/10.1021/acsami.1c09019
ACS Appl. Mater. Interfaces XXXX, XXX, XXX−XXX

appeared in the cycled [**(NPr)$_2$PV**]**·4Cl** anolyte, confirming the crossover of TEMPO species (Figure S16). Furthermore, in high-resolution electrospray ionization mass spectrometry (HRESIMS), the signals of TEMPO species were detected in the [**(NPr)$_2$PV**]**·4Cl** anolyte after galvanostatic cycling (Figure S17), matching well with our NMR and CV results. Compared with the conventional galvanostatic cycling, the galvanostatic cycling with potential holds after each half-cycle ends would lead to more apparent crossover and decomposition of N^{Me}-TEMPO, which is the reason why it showed a faster capacity fate rate (Figures S14 and S15).

The reason why the alkyl-chain cleaved decomposition compound of [**(NPr)$_2$PV**]**·4Cl** is hardly detected in the cycled anolyte is because the introduction of a phenylene group can warrant a certain degree of large π-conjugation effects and mitigate the intramolecular Coulombic repulsion between the two positively charged pyridinium centers, thus helping to enhance the electrochemical stability of AORFBs. Moreover, when the charge voltage was limited to 1.73 V, the AORFB delivered a slower capacity degradation with a fade rate of 0.025% per cycle over 500 cycles and 2.68% per day (Figure S18), suggesting that the lower upper limit of charge voltage could bring forth more durable cycling performance.

To clarify the two single-electron reduction processes of [**(NPr)$_2$PV**]**·4Cl**, a series of spectroscopic techniques were conducted at different charging states of the [**(NPr)$_2$PV**]**·4Cl** anolyte. No-deuterium nuclear magnetic resonance (No-D NMR) spectroscopy was performed by taking the sample from the [**(NPr)$_2$PV**]**·4Cl** anolytes at different charging states with a sealed capillary containing D_2O as a reference deuterated solvent (Figure 4a and Figure S19).[51] Compared with the conventional NMR method, No-D NMR spectroscopy can reflect the intrinsic signals of [**(NPr)$_2$PV**]**·4Cl** due to not being contaminated by the deuterated solvent. During the charging process, the signals of the aromatic rings of [**(NPr)$_2$PV**]**·4Cl** broadened and shifted upfield and then disappeared (Figure S13a), demonstrating the efficient shielding by the formed radicals. Moreover, the shift in water solvent resonance could reflect the change in the magnetic susceptibility of the solution.[52] When the anolyte was charged from a pristine state to 1.90 V, the position of the water peak increased from 4.39 to 4.45 ppm and then decreased to 4.43 ppm, which indicates that the concentration of formed radicals first increased and then decreased, revealing the two single-electron reductions of [**(NPr)$_2$PV**]$^{4+}$ and the presence of the quinoid form [**(NPr)$_2$PV**]$^{2+}$ at the fully charged state. Furthermore, during the charging process, the characteristic peak of the ammonium groups in [**(NPr)$_2$PV**]$^{4+}$ (marked as "α" in Figure 4b) shifted downfield from 2.99 to 3.02 ppm and then shifted upfield to 2.86 ppm. Additionally, the signals attributed to the alkyl chains of [**(NPr)$_2$PV**]$^{4+}$ (marked as "β" in Figure 4b) remarkably shifted downfield from 2.44 to 3.05 ppm when charged to 1.70 V and then slightly upshifted to 3.02 ppm when further charged to1.90 V. This is because the alkyl ammonium groups away from the pyridinium rings are more susceptible to the aqueous environment than the generated free radicals on the aromatic rings during the charge process. Thus, the variation tendency of α or β signals in the ^{1}H NMR chemical shift is similar to that of the water peak with an initial downfield shift and then an upfield shift, suggesting the two single-electron reductions and the generation of the quinoid form. We propose that the two dynamic single-electron redox reactions of [**(NPr)$_2$PV**]$^{2+}$ made a significant contribution to the enhanced redox reversibility, thus resulting in a stable cycling life of the [**(NPr)$_2$PV**]**·4Cl**/N^{Me}-TEMPO AORFBs.

Furthermore, EPR spectroscopy was employed to monitor the formation and concentration variation of free radicals in the [**(NPr)$_2$PV**]**·4Cl** anolyte at different charge states.[53] The EPR spectrum of the pristine [**(NPr)$_2$PV**]**·4Cl** anolyte displayed almost no signal. When charged to 1.70 V, there was a significant increase in the EPR intensity, demonstrating the formation of free radicals (Figure 4c). However, after charging to 1.75 V, a remarkable decrease in the EPR response was observed. The EPR signal became very weak when charged to 1.90 V, demonstrating that the monoradical form [**(NPr)$_2$PV**]$^{3+}$ was nearly totally consumed, and the final quinoid form [**(NPr)$_2$PV**]$^{2+}$ was the dominant species in the fully charged state. During the charging process, the increase and then decrease in the EPR response confirmed the formation of the monoradical form [**(NPr)$_2$PV**]$^{3+}$ and then the quinoid form [**(NPr)$_2$PV**]$^{2+}$, demonstrating the occurrence of two single-electron reductions.

The charging process of the [**(NPr)$_2$PV**]**·4Cl** anolyte is accompanied by strong color shifts from yellow to brown and finally to purple, which provides a visible indication of the state of charge and also indicates the two single-electron reductions of [**(NPr)$_2$PV**]**·4Cl** (Figure S20). As revealed by the UV−vis absorption spectra (Figure 4d), two peaks at 464.7 and 510.8 nm emerged when charged to 1.60 V, while the intensity of the absorption band at 322.6 nm (attributable to [**(NPr)$_2$PV**]$^{4+}$) decreased, indicating the consumption of [**(NPr)$_2$PV**]$^{4+}$ and the formation of monoradical [**(NPr)$_2$PV**]$^{3+}$. When charged to 1.75 V, a new peak at 547.9 nm appeared, and its intensity gradually increased during further charging, demonstrating the formation of [**(NPr)$_2$PV**]$^{2+}$ after the second electron reduction. It should be noticed that the weak remaining absorption peaks of [**(NPr)$_2$PV**]$^{4+}$ and monoradical [**(NPr)$_2$PV**]$^{3+}$ after charging to 1.90 V are due to unavoidable air exposure during ex situ UV−vis absorption tests, which does not mean that the two single-electron reductions of [**(NPr)$_2$PV**]$^{4+}$ cannot be completely processed. Overall, the above spectroscopic results revealed that two successive single-electron reductions occurred from [**(NPr)$_2$PV**]$^{4+}$ to [**(NPr)$_2$PV**]$^{3+}$ and then finally to [**(NPr)$_2$PV**]$^{2+}$, whose quinoid form should be the dominant species in the fully charged state.

3. CONCLUSIONS

In conclusion, molecular engineering of an extended and cationized bipyridine was established for significantly lowering the redox potential of the two-electron-storage anolyte. The bridging phenylene group in the π-conjugation-extended bipyridine, [**(NPr)$_2$PV**]**·4Cl**, plays a dual role. First, it prevents communication between the two pyridinium redox centers, thus providing an extremely low redox potential (−0.77 V vs SHE, 2e$^-$). Second, it warrants a certain degree of π conjugation and mitigates the intramolecular Coulombic repulsion between the two positively charged pyridinium centers, thus helping to enhance the electrochemical stability. When paired with N^{Me}-TEMPO as the catholyte, [**(NPr)$_2$PV**]**·4Cl** enabled an unprecedentedly high cell voltage up to 1.71 V for pH-neutral AORFBs. The high-voltage [**(NPr)$_2$PV**]**·4Cl**/N^{Me}-TEMPO AORFBs could deliver long-term reversible cycling with a capacity retention of 99.94% per cycle, an ultrahigh energy efficiency of ~89%, and a Coulombic

https://doi.org/10.1021/acsami.1c09019

efficiency of ~100%. To the best of our knowledge, the battery performance data presented here are among the best results of existing pH-neutral AORFB systems (Table S1). Importantly, the two single-electron reductions of $[(\mathbf{NPr})_2\mathbf{PV}]\cdot\mathbf{4Cl}$, which underwent transformation from the initial cationic form to the monoradical form ($[(\mathbf{NPr})_2\mathbf{PV}]^{4+} \rightarrow [(\mathbf{NPr})_2\mathbf{PV}]^{3+}$) and then to the quinoid form ($[(\mathbf{NPr})_2\mathbf{PV}]^{3+} \rightarrow [(\mathbf{NPr})_2\mathbf{PV}]^{2+}$) during the charging process, were clarified by No-D NMR and other spectroscopic techniques. We anticipate that this work will bring inspiration to rational molecular design and redox variation probing of organic species for developing advanced high-voltage stable AORFBs.

4. EXPERIMENTAL SECTION

4.1. Chemicals and Materials. All reagents were purchased from commercial sources, stored in a refrigerator (2 °C) or in a desiccator, and used as received unless otherwise stated. N^{Me}-TEMPO and (3-bromopropyl)-trimethyl-ammonium bromide were prepared according to previous studies.[21,54] The preparations of **PhPy**, $[(\mathbf{NPr})_2\mathbf{PV}]\cdot\mathbf{4Cl}$, and **MPV·2Cl** (control sample) are as follows:

*4.1.1. Preparation of **PhPy**.* Typically, 4-pyridineboronic acid pinacol ester (4.26 g, 20.78 mmol), 1,4-dibromobenzene (2.04 g, 8.65 mmol), $Pd(PPh_3)_4$ (0.999 g, 0.865 mmol), and K_3PO_4 (18.50 g, 87.16 mmol) were added to a mixture of dimethyl formamide (DMF) and 1,4-dioxane (dry and degassed, 100 mL, 1:1 in volume). The reaction mixture was heated at 130 °C in a N_2 atmosphere for 48 h, cooled to room temperature, and then filtered. The solid residue was washed with CH_2Cl_2. The combined organic filtrate was concentrated under vacuum and then dissolved in CH_2Cl_2 followed by three extractions with H_2O. Then, concentrated HCl (approximately 2.0 mL) was added to the organic phase, resulting in the precipitation of the desired product from the solution. The precipitate was collected by filtration and then dissolved in H_2O. Finally, aqueous NaOH solution (10 M) was added dropwise to the above solution until the pH was in the range of 8−9, which resulted in the precipitation of the pure product **PhPy** as a white solid (1.81 g, yield 90.1%). ^1H NMR (400 MHz, $CDCl_3$, 25 °C): δ 8.71 (dd, J = 4.5, 1.6 Hz, 4H), 7.78 (s, 4H), 7.56 (dd, J = 4.5, 1.6 Hz, 4H). ^{13}C NMR (100 MHz, $CDCl_3$, 25 °C): δ 150.4, 147.4, 138.8, 127.8, 121.6.

4.1.2. Preparation of $[(NPr)_2PV]\cdot 4Cl$. In a 100 mL round-bottom flask, **PhPy** (0.50 g, 2.15 mmol) and (3-bromopropyl)-trimethyl-ammonium bromide (2.25 g, 8.62 mmol) were added to 50 mL of DMF and stirred at 100 °C for 3 days under a N_2 atmosphere. The resulting light-yellow precipitate was filtered, suspended in DMF (20 mL) at 100 °C, and stirred for 15 min. This process was repeated three times. Finally, the precipitate was filtered and washed with CH_3CN (3 × 20 mL) and then dried under vacuum at 80 °C to obtain $[(\mathbf{NPr})_2\mathbf{PV}]\cdot\mathbf{4Br}$ as a white solid. ^1H NMR (400 MHz, D_2O, 25 °C): δ 8.83 (d, J = 7.0 Hz, 4H), 8.32 (d, J = 7.0 Hz, 4H), 8.04 (s, 4H), 4.62 (t, J = 7.7 Hz, 4H), 3.44−3.40 (m, 4H), 3.20 (s, 18H), 2.55−2.47 (m, 4H). ^{13}C NMR (100 MHz, D_2O, 25 °C): δ 155.8, 144.5, 137.0, 129.3, 125.9, 62.5, 57.4, 53.3, 24.6. Subsequently, the Br^- ions of $[(\mathbf{NPr})_2\mathbf{PV}]\cdot\mathbf{4Br}$ were exchanged by Cl^- ions with an anion exchange column (Amberlite IRA-900 chloride form resin) to obtain $[(\mathbf{NPr})_2\mathbf{PV}]\cdot\mathbf{4Cl}$ as a white solid (1.04 g, 84.2%). CV analysis was applied to validate the complete removal of Br^- ions. ^1H NMR (400 MHz, D_2O, 25 °C): δ 8.81 (d, J = 7.0 Hz, 4H), 8.32 (d, J = 7.0 Hz, 4H), 8.04 (s, 4H), 4.61 (t, J = 7.7 Hz, 4H), 3.43−3.39 (m, 4H), 3.04 (s, 18H), 2.54−2.46 (m, 4H). ^{13}C NMR (100 MHz, D_2O, 25 °C): δ 155.9, 144.5, 137.0, 129.3, 125.9, 62.5, 57.3, 53.1, 24.5. HRESIMS for $[(\mathbf{NPr})_2\mathbf{PV}]\cdot\mathbf{4Cl}$, calcd. for $C_{28}H_{42}Cl_4N_4$: m/z = 108.5847 $[M - 4Cl]^{4+}$, 252.1388 $[M - 2Cl]^{2+}$; found: 108.5850 $[M - 4Cl]^{4+}$, 252.1387 $[M - 2Cl]^{2+}$.

*4.1.3. Preparation of **MPV·2Cl** (Control Sample).* A CH_3CN (50 mL) solution of **PhPy** (500 mg, 2.15 mmol) was introduced into a round-bottom flask (100 mL), and excess CH_3I (0.60 mL, 9.64 mmol) was added to the flask and stirred at 60 °C under a N_2 atmosphere for 6 h.[55] The reaction mixture was cooled to room temperature, and the resulting precipitate was filtered and washed multiple times with hexane to remove the unreacted CH_3I. The crude product was further dried under vacuum at 80 °C for 12 h to obtain **MPV·2I** as a yellow solid. The anion-exchange method was used to replace I^- ions with Cl^- ions. First, **MPV·2I** was dissolved in H_2O and reprecipitated by adding an excess NH_4PF_6 salt. Next, the precipitate was filtered and washed with H_2O and dried in air, yielding $\mathbf{MPV\cdot 2PF_6}$ as a yellow solid. Then, $\mathbf{MPV\cdot 2PF_6}$ was dissolved in CH_3CN and reprecipitated by adding an excess tetrabutylammonium chloride (TBACl) salt. The precipitate was collected by filtration, washed with CH_3CN and CH_2Cl_2, and then dried in air to yield **MPV·2Cl** as a white solid (693 mg, yield 96.6%). ^1H NMR (400 MHz, D_2O, 25 °C): δ 8.68 (d, J = 6.8 Hz, 4H), 8.23 (d, J = 7.0 Hz, 4H), 8.01 (s, 4H), 4.26 (s, 6H). ^{13}C NMR (100 MHz, D_2O, 25 °C): δ 154.6, 145.2, 136.8, 129.0, 125.1, 47.5.

4.2. Electrochemical Studies. All the CV and LSV experiments were carried out in 0.5 M NaCl supporting electrolytes with a CHI-760E workstation (Chenhua Instruments, China). All potentials were referenced to SHE according to the known $MV^{2+/1+}$ redox couple (−0.45 V vs SHE).[13] The working electrode (glassy carbon) was polished using Al_2O_3 powder (50 nm dimeter) suspended in deionized H_2O, rinsed with deionized H_2O, and dried with an air flow. The Ag/AgCl reference electrode was suspended in a solution of a 0.5 M NaCl electrolyte. A Pt wire was used as the counter electrode. For the CV studies, a 3 mm glassy carbon electrode (GC-130, China) was used as the working electrode. For LSV studies, a 5 mm glassy carbon rotating disk electrode was used as the working electrode. The LSV scans were collected with a rotation speed from 300 to 2400 rpm at a rate of 5 mV s^{-1} from −0.65 to −0.93 V vs SHE, which were recorded three times at each rotation rate to ensure accuracy. The limiting current at each rotation rate was recorded at −0.90 V vs SHE. Due to the overlap of the two single-electron reductions of $[(\mathbf{NPr})_2\mathbf{PV}]\cdot\mathbf{4Cl}$, the diffusion coefficient (D) and the kinetic rate constant (k_0) were calculated from the Levich equation and the Tafel equation, respectively. The corresponding slope from the linear relationship was transformed using the following Levich equation to obtain a D value of 2.58(4) × 10^{-6} cm^2 s^{-1} for $[(\mathbf{NPr})_2\mathbf{PV}]^{4+}$

$$\text{Levich plot slope} = 0.620 \times \text{nFAcD}^{2/3}\nu^{-1/6} \quad (1)$$

where n is the electron number (2 in this case), F is the Faraday's constant (96,485 C mol^{-1}), A is the electrode area (0.1963 cm^2), c is the concentration of $[(\mathbf{NPr})_2\mathbf{PV}]\cdot\mathbf{4Cl}$ (1 × 10^{-6} mol cm^{-3}), and ν is the kinematic viscosity of a 0.5 M NaCl solution (0.009 cm^2 s^{-1}). The Tafel equation can be written as the following equation

$$\log_{10}|i_k| = \log_{10}|\text{nFcAk}_0| + \alpha nF\eta/(2.303 \times RT) \quad (2)$$

where the parameters including n, F, c, and A are the same as those in eq 1, k_0 is the rate constant, α is the charge transfer coefficient, η is the overpotential, R is the universal gas constant (8.314 J K^{-1}), T is the temperature (293.15 K), and i_k is the mass transfer-independent current (the extrapolation to an infinite rotation rate). The reciprocal of i_k is calculated from the Koutecký−Levich equation (current^{-1} vs $\text{rotation rate}^{-1/2}$) by the extrapolation to an infinite rotation rate.

4.3. Flow Battery Tests. The AORFBs were constructed with two graphite chambers (7 cm × 7 cm × 1 cm) carved with serpentine fluid channels, two graphite felt electrodes (with an active area of 5 cm^2), a piece of an anion-exchange membrane (AMV, 120 μm thickness, pore size of <10 Å, Selemion, Japan), and two corrosive-resistant Ti current collectors to avoid possible corrosion from the electrolyte. Each graphite chamber was connected with an electrolyte reservoir using PTFE tubes. A two-channel *L/S* peristaltic pump (BR600, Zibo Newkai Electromechanical Equipment Co., Ltd.) was used with Viton tubing for circulating the electrolytes through the electrodes at a flow rate of 60 mL min^{-1}. The anolyte is 0.1 M $[(\mathbf{NPr})_2\mathbf{PV}]\cdot\mathbf{4Cl}$ in 5.0 mL of a 2.0 M NaCl aqueous solution. The catholyte is 0.2 M N^{Me}-TEMPO in 7.5 mL of a 2.0 M NaCl aqueous solution. The AORFBs were also tested at a higher concentration of 0.5 M $[(\mathbf{NPr})_2\mathbf{PV}]\cdot\mathbf{4Cl}$ in 5.0 mL of a 2.0 M NaCl aqueous solution and 1.0 M N^{Me}-TEMPO in 7.5 mL of a 2.0 M NaCl aqueous solution.

All the prepared anolytes and catholytes were ultrasonicated for 1 h before battery tests to remove most of the dissolved O_2 in the solution. The reservoirs were purged with N_2 to remove O_2 in the system and then sealed. The charge−discharge performances of $[(\mathbf{NPr})_2\mathbf{PV}]\cdot\mathbf{4Cl}$/N^{Me}-TEMPO AORFBs were tested in a N_2-filled glovebox with a LAND-CT3001A multichannel battery test system at room temperature.

4.4. Spectroscopic Analyses. The ^{1}H NMR and ^{13}C NMR spectra were recorded on a Bruker Advance III 400 spectrometer with the deuterated solvent as the lock and the residual solvent or $(CH_3)_4Si$ as the internal reference. No-D NMR spectroscopy was conducted by adding a sealed capillary filled with D_2O into the sample tube to prevent direct contact between the sample and the deuterated solvent. The samples for No-D NMR tests were taken from the $[(\mathbf{NPr})_2\mathbf{PV}]\cdot\mathbf{4Cl}$ anolytes at different charge states, sealed with a parafilm in a N_2-filled glovebox, and then immediately tested to obtain ^{1}H NMR spectra. The HRESIMS spectra were obtained on a Thermo Fisher Scientific Q Exactive high-resolution mass spectrometer equipped with an electrospray ionization probe. UV−vis absorption profiles were collected on a UV-2600 spectrometer (Shimadzu Corp.), and the light path length is 1 cm or 1 mm. EPR spectra were obtained using a Bruker EMX plus-6/1 variable-temperature apparatus. The EPR samples were sealed in a quartz capillary and detected at room temperature immediately without adding any free-radical-catching agent.

4.5. Solubility Tests. The solubilities of the samples were determined by UV−vis spectroscopy. For example, the experimental procedure for determining the solubility of $[(\mathbf{NPr})_2\mathbf{PV}]\cdot\mathbf{4Cl}$ is as follows: First, a 5 mM sample was dissolved in 5 mL of aqueous solution (in water or in 2 M NaCl solution) and then diluted to the concentrations of 4, 8, 12, 16, and 20 μM in aqueous solution. Second, the standard curve based on UV−vis spectroscopy was established with the sample concentrations of 4, 8, 12, 16, and 20 μM. Third, the saturated aqueous solution of the sample was prepared by adding the solvent until the sample was completely dissolved and then progressively diluted to 125,000 times (10 μL of saturated solution was taken out by a pipettor and diluted to a 5 mL aqueous solution, 20 μL of which was further taken out and again diluted to a 5 mL aqueous solution). As a result, the saturated concentration of $[(\mathbf{NPr})_2\mathbf{PV}]\cdot\mathbf{4Cl}$ can be calculated and obtained. Similarly, the solubility data of **MPV·2Cl** (control sample) can be obtained by using the same method.

4.6. Calculations. The calculations of the theoretical energy density for a battery, the theoretical volumetric capacity, and the g factor for EPR spectroscopy are as follows:

4.6.1. The Theoretical Energy Density for a Full Battery. For the full cell, the theoretical energy density of the $[(\mathbf{NPr})_2\mathbf{PV}]\cdot\mathbf{4Cl}$/N^{Me}-TEMPO AORFB was calculated using the following equation

$$\text{energy density (W h/L)} = \text{nCFV}/\mu_\nu \tag{3}$$

where n is the electron number involved in the redox reaction (2 in this case), C is the lower concentration of the active material, F is the Faraday's constant (26.8 Ah mol^{-1}), V is the cell voltage, and μ_ν is the volume factor (μ_ν = 1 + lower electrolyte concentration/higher electrolyte concentration).[31] The solubility of $[(\mathbf{NPr})_2\mathbf{PV}]\cdot\mathbf{4Cl}$ in H_2O was measured to be 1.29 M and used for calculation. The solubility of N^{Me}-TEMPO was measured to be 3.0 M (corresponding to 1.5 M for two-electron storage). For the $[(\mathbf{NPr})_2\mathbf{PV}]\cdot\mathbf{4Cl}$/N^{Me}-TEMPO AORFBs, μ_ν = 1 + 1.29/1.5 = 1.86; accordingly, its energy density is calculated to be (2 × 1.29 × 26.8 × 1.71)/1.86 = 63.6 W h L^{-1}.

4.6.2. Calculation of the Theoretical Volumetric Capacity. The theoretical volumetric capacity of $[(\mathbf{NPr})_2\mathbf{PV}]\cdot\mathbf{4Cl}$/N^{Me}-TEMPO AORFBs was calculated using the following equation

$$\text{theoretical volumetric capacity} = 26.806 \times nc(\text{A h L}^{-1}) \tag{4}$$

where n is the number of charges stored in each active molecule and c is the molar concentration of the active molecule (mol L^{-1}).

4.6.3. Calculation of the g Factor for EPR Spectroscopy. The so-called g factor of an electron was calculated from the following equation

$$g = h\nu/(\beta B) \tag{5}$$

where h is the Planck's constant (equal to 6.626 × 10^{-27} erg·s), ν is the microwave frequency (equal to 9.85 GHz), β is the Bohr magneton (equal to 9.274 × 10^{-21} erg·G^{-1}), and B is the magnetic field strength, which is obtained from Figure 4c.

■ ASSOCIATED CONTENT

Supporting Information

The Supporting Information is available free of charge at https://pubs.acs.org/doi/10.1021/acsami.1c09019.

> Supporting data including NMR spectra, UV−vis analyses, CV curves, schematics of the AORFB configuration, battery performances, HRESIMS spectra, and photographs (Figures S1−S20) and performance comparisons (Table S1) (PDF)

■ AUTHOR INFORMATION

Corresponding Author

Zhong Jin − *MOE Key Laboratory of Mesoscopic Chemistry, MOE Key Laboratory of High Performance Polymer Materials and Technology, Jiangsu Key Laboratory of Advanced Organic Materials, School of Chemistry and Chemical Engineering, Nanjing University, Nanjing 210023, China; Shenzhen Research Institute of Nanjing University, Shenzhen 518057, China;* orcid.org/0000-0001-8860-8579; Email: zhongjin@nju.edu.cn

Authors

Mingguang Pan − *MOE Key Laboratory of Mesoscopic Chemistry, MOE Key Laboratory of High Performance Polymer Materials and Technology, Jiangsu Key Laboratory of Advanced Organic Materials, School of Chemistry and Chemical Engineering, Nanjing University, Nanjing 210023, China*

Yan Lu − *MOE Key Laboratory of Mesoscopic Chemistry, MOE Key Laboratory of High Performance Polymer Materials and Technology, Jiangsu Key Laboratory of Advanced Organic Materials, School of Chemistry and Chemical Engineering, Nanjing University, Nanjing 210023, China*

Shuyu Lu − *MOE Key Laboratory of Mesoscopic Chemistry, MOE Key Laboratory of High Performance Polymer Materials and Technology, Jiangsu Key Laboratory of Advanced Organic Materials, School of Chemistry and Chemical Engineering, Nanjing University, Nanjing 210023, China*

Bo Yu − *MOE Key Laboratory of Mesoscopic Chemistry, MOE Key Laboratory of High Performance Polymer Materials and Technology, Jiangsu Key Laboratory of Advanced Organic Materials, School of Chemistry and Chemical Engineering, Nanjing University, Nanjing 210023, China*

Jie Wei − *MOE Key Laboratory of Mesoscopic Chemistry, MOE Key Laboratory of High Performance Polymer Materials and Technology, Jiangsu Key Laboratory of Advanced Organic Materials, School of Chemistry and Chemical Engineering, Nanjing University, Nanjing 210023, China*

Yuzhu Liu − *MOE Key Laboratory of Mesoscopic Chemistry, MOE Key Laboratory of High Performance Polymer*

Materials and Technology, Jiangsu Key Laboratory of Advanced Organic Materials, School of Chemistry and Chemical Engineering, Nanjing University, Nanjing 210023, China

Complete contact information is available at:
https://pubs.acs.org/10.1021/acsami.1c09019

Notes

The authors declare no competing financial interest.

■ ACKNOWLEDGMENTS

This work was financially supported by the National Key Research and Development Program of China (2017YFA0208200), the Fundamental Research Funds for the Central Universities of China (0205-14380266), the Natural Science Foundation of China (22022505 and 21872069), the Natural Science Foundation of Jiangsu Province (BK20180008 and BK20200306), and the Shenzhen Fundamental Research Program of Science, Technology and Innovation Commission of Shenzhen Municipality (JCYJ20180307155007589).

■ REFERENCES

(1) Park, M.; Ryu, J.; Wang, W.; Cho, J. Material Design and Engineering of Next-Generation Flow-Battery Technologies. *Nat. Rev. Mater.* **2017**, *2*, 16080.

(2) Dunn, B.; Kamath, H.; Tarascon, J.-M. Electrical Energy Storage for the Grid: A Battery of Choices. *Science* **2011**, *334*, 928−935.

(3) Yang, Z.; Zhang, J.; Kintner-Meyer, M. C. W.; Lu, X.; Choi, D.; Lemmon, J. P.; Liu, J. Electrochemical Energy Storage for Green Grid. *Chem. Rev.* **2011**, *111*, 3577−3613.

(4) Soloveichik, G. L. Flow Batteries: Current Status and Trends. *Chem. Rev.* **2015**, *115*, 11533−11558.

(5) Huskinson, B.; Marshak, M. P.; Suh, C.; Er, S.; Gerhardt, M. R.; Galvin, C. J.; Chen, X.; Aspuru-Guzik, A.; Gordon, R. G.; Aziz, M. J. A Metal-Free Organic-Inorganic Aqueous Flow Battery. *Nature* **2014**, *505*, 195−198.

(6) Yao, Y.; Lei, J.; Shi, Y.; Ai, F.; Lu, Y.-C. Assessment Methods and Performance Metrics for Redox Flow Batteries. *Nat. Energy* **2021**, *6*, 582−588.

(7) Kwabi, D. G.; Ji, Y.; Aziz, M. J. Electrolyte Lifetime in Aqueous Organic Redox Flow Batteries: A Critical Review. *Chem. Rev.* **2020**, *120*, 6467−6489.

(8) Feng, R.; Zhang, X.; Murugesan, V.; Hollas, A.; Chen, Y.; Shao, Y.; Walter, E.; Wellala, N. P. N.; Yan, L.; Rosso, K. M.; Wang, W. Reversible Ketone Hydrogenation and Dehydrogenation for Aqueous Organic Redox Flow Batteries. *Science* **2021**, *372*, 836−840.

(9) Yang, B.; Hoober-Burkhardt, L.; Wang, F.; Prakash, G. K. S.; Narayanan, S. R. An Inexpensive Aqueous Flow Battery for Large-Scale Electrical Energy Storage Based on Water-Soluble Organic Redox Couples. *J. Electrochem. Soc.* **2014**, *161*, A1371−A1380.

(10) Janoschka, T.; Martin, N.; Martin, U.; Friebe, C.; Morgestern, S.; Hiller, H.; Hager, M. D.; Schubert, U. S. An Aqueous, Polymer-Based Redox-flow Battery Using Non-corrosive, Safe, and Low-Cost Materials. *Nature* **2015**, *527*, 78−81.

(11) Lin, K.; Chen, Q.; Gerhart, M. R.; Tong, L.; Kim, S. B.; Eisenach, L.; Valle, A. W.; Hardee, D.; Gordon, R. G.; Aziz, M. J.; Marshak, M. P. Alkaline Quinone Flow Battery. *Science* **2015**, *349*, 1529−1532.

(12) Lin, K.; Gómez-Bombarelli, R.; Beh, E. S.; Tong, L.; Chen, Q.; Valle, A.; Aspuru-Guzik, A.; Aziz, M. J.; Gordon, R. G. A Redox-Flow Battery with an Alloxazine-Based Organic Electrolyte. *Nat. Energy* **2016**, *1*, 16102.

(13) Liu, T.; Wei, X.; Nie, Z.; Sprenkle, V.; Wang, W. A Total Organic Aqueous Redox Flow Battery Employing a Low Cost and Sustainable Methyl Viologen Anolyte and 4-HO-TEMPO Catholyte. *Adv. Energy Mater.* **2016**, *6*, 1501449.

(14) Wang, W.; Sprenkle, V. Redox Flow Batteries Go Organic. *Nat. Chem.* **2016**, *8*, 204−206.

(15) Li, Z.; Lu, Y.-C. Polysulfide-Based Redox Flow Batteries with Long Life and Low Levelized Cost Enabled by Charge-Reinforced Ion-Selective Membranes. *Nat. Energy* **2021**, *6*, 517−528.

(16) Zhang, L.; Qian, Y.; Feng, R.; Ding, Y.; Zu, X.; Zhang, C.; Guo, X.; Wang, W.; Yu, G. Reversible Redox Chemistry in Azobenzene-Based Organic Molecules for High-capacity and Long-life Non-aqueous Redox Flow Batteries. *Nat. Commun.* **2020**, *11*, 3843.

(17) Winsberg, J.; Hagemann, T.; Janoschka, T.; Hager, M. D.; Schubert, U. S. Redox-Flow Batteries: From Metals to Organic Redox-Active Materials. *Angew. Chem., Int. Ed.* **2017**, *56*, 686−711.

(18) Zhang, L.; Zhang, C.; Ding, Y.; Ramirez-Meyers, K.; Yu, G. A Low-Cost and High-Energy Hybrid Iron-Aluminum Liquid Battery Achieved by Deep Eutectic Solvents. *Joule* **2017**, *1*, 623−633.

(19) Ding, Y.; Zhang, C.; Zhang, L.; Zhou, Y.; Yu, G. Molecular Engineering of Organic Electroactive Materials for Redox Flow Batteries. *Chem. Soc. Rev.* **2018**, *47*, 69−103.

(20) Janoschka, T.; Martin, N.; Hager, M. D.; Schubert, U. S. An Aqueous Redox-Flow Battery with High Capacity and Power: The TEMPTMA/MV System. *Angew. Chem., Int. Ed.* **2016**, *55*, 14427−14430.

(21) DeBruler, C.; Hu, B.; Moss, J.; Liu, X.; Luo, J.; Sun, Y.; Liu, T. L. Designer Two-Electron Storage Viologen Anolyte Materials for Neutral Aqueous Organic Redox Flow Batteries. *Chem* **2017**, *3*, 961−978.

(22) Luo, J.; Hu, B.; Debruler, C.; Liu, T. L. A Π-Conjugation Extended Viologen as a Two-Electron Storage Anolyte for Total Organic Aqueous Redox Flow Batteries. *Angew. Chem., Int. Ed.* **2018**, *57*, 231−235.

(23) DeBruler, C.; Hu, B.; Moss, J.; Luo, J.; Liu, T. L. A Sulfonate-Functionalized Viologen Enabling Neutral Cation Exchange, Aqueous Organic Redox Flow Batteries toward Renewable Energy Storage. *ACS Energy Lett.* **2018**, *3*, 663−668.

(24) Jin, S.; Fell, E. M.; Vina-Lopez, L.; Jing, Y.; Michalak, P. W.; Gordon, R. G.; Aziz, M. J. Near Neutral pH Redox Flow Battery with Low Permeability and Long-Lifetime Phosphonated Viologen Active Species. *Adv. Energy Mater.* **2020**, *10*, 2000100.

(25) Hu, B.; Luo, J.; Hu, M.; Yuan, B.; Liu, T. L. A pH-Neutral, Metal-Free Aqueous Organic Redox Flow Battery Employing an Ammonium Anthraquinone Anolyte. *Angew. Chem., Int. Ed.* **2019**, *58*, 16629−16636.

(26) Yan, W.; Wang, C.; Tian, J.; Zhu, G.; Ma, L.; Wang, Y.; Chen, R.; Hu, Y.; Wang, L.; Chen, T.; Ma, J.; Jin, Z. All-Polymer Particulate Slurry Batteries. *Nat. Commun.* **2019**, *1*, 2513.

(27) Zhou, M.; Chen, Y.; Salla, M.; Zhang, H.; Wang, X.; Mothe, S. R.; Wang, Q. Single-Molecule Redox-Targeting Reactions for a pH-Neutral Aqueous Organic Redox Flow Battery. *Angew. Chem., Int. Ed.* **2020**, *59*, 14286−14291.

(28) Kwabi, D. G.; Lin, K.; Ji, Y.; Kerr, E. F.; Goulet, M.-A.; Porcellinis, D. D.; Tabor, D. P.; Pollack, D. A.; Aspuru-Guzik, A.; Gordon, R. G.; Aziz, M. J. Alkaline Quinone Flow Battery with Long Lifetime at pH 12. *Joule* **2018**, *2*, 1894−1906.

(29) Ji, Y.; Goulet, M.-A.; Pollack, D. A.; Kwabi, D. G.; Jin, S.; Porcellinis, D. D.; Kerr, E. F.; Gordon, R. G.; Aziz, M. J. A Phosphonate-Functionalized Quinone Redox Flow Battery at Near-Neutral pH with Record Capacity Retention Rate. *Adv. Energy Mater.* **2019**, *9*, 190039.

(30) Liu, Y.; Goulet, M.-A.; Tong, L.; Liu, Y.; Ji, Y.; Wu, L.; Gordon, R. G.; Aziz, M. J.; Yang, Z.; Xu, T. A Long-Lifetime All-Organic Aqueous Flow Battery Utilizing TMAP-TEMPO Radical. *Chem* **2019**, *5*, 1861−1870.

(31) Hu, B.; Debruler, C.; Rhodes, Z.; Liu, T. L. Long-Cycling Aqueous Organic Redox Flow Battery (AORFB) toward Sustainable and Safe Energy Storage. *J. Am. Chem. Soc.* **2017**, *139*, 1207−1214.

(32) Beh, E. S.; Porcellinis, D. D.; Gracia, R. L.; Xia, K. T.; Gordon, R. G.; Aziz, M. J. A Neutral pH Aqueous Organic−Organometallic

Redox Flow Battery with Extremely High Capacity Retention. *ACS Energy Lett.* **2017**, *2*, 639−644.

(33) Zhang, C.; Qian, Y.; Ding, Y.; Zhang, L.; Guo, X.; Zhao, Y.; Yu, G. Biredox Eutectic Electrolytes Derived from Organic Redox-active Molecules: High-Energy Storage Systems. *Angew. Chem., Int. Ed.* **2019**, *58*, 7045−7050.

(34) Orita, A.; Verde, M. G.; Sakai, M.; Meng, Y. S. A Biomimetic Redox Flow Battery Based on Flavin Mononucleotide. *Nat. Commun.* **2016**, *7*, 13230.

(35) Hollas, A.; Wei, X.; Murugesan, V.; Nie, Z.; Li, B.; Reed, D.; Liu, J.; Sprenkle, V.; Wang, W. A Biomimetic High-Capacity Phenazine-Based Anolyte for Aqueous Organic Redox Flow Batteries. *Nat. Energy* **2018**, *3*, 508−514.

(36) Zu, X.; Zhang, L.; Qian, Y.; Zhang, C.; Yu, G. Molecular Engineering of Azobenzene-Based Anolytes towards High-Capacity Aqueous Redox Flow Batteries. *Angew. Chem., Int. Ed.* **2020**, *59*, 2−22170.

(37) Sevov, C. S.; Hickey, D. P.; Cook, M. E.; Robinson, S. G.; Barnett, S.; Minteer, S. D.; Sigman, M. S.; Sanford, M. S. Physical Organic Approach to Persistent, Cyclable, Low-Potential Electrolytes for Flow Battery Applications. *J. Am. Chem. Soc.* **2017**, *139*, 2924−2927.

(38) Park, M.; Beh, E. S.; Fell, E. M.; Jing, Y.; Kerr, E. F.; Porcellinis, D. D.; Goulet, M.-A.; Ryu, J.; Wong, A. A.; Gordon, R. G.; Cho, J.; Aziz, M. J. A High Voltage Aqueous Zinc−Organic Hybrid Flow Battery. *Adv. Energy Mater.* **2019**, *9*, 1900694.

(39) Liu, L.; Yao, Y.; Wang, Z.; Lu, Y.-C. Viologen Radical Stabilization by Molecular Spectators for Aqueous Organic Redox Flow Batteries. *Nano Energy* **2021**, *84*, 105897.

(40) Leung, P.; Martin, T.; Xu, Q.; Flox, C.; Mohamad, M. R.; Palma, J.; Rodchanarowan, A.; Zhu, X.; Xing, W. W.; Shah, A. A. A New Aqueous All-Organic Flow Battery with High Cell Voltage in Acidic Electrolytes. *Applied Energy* **2021**, *282*, 116058.

(41) Hu, P.; Lan, H.; Wang, X.; Yang, Y.; Liu, X.; Wang, H.; Guo, L. Renewable-Lawsone-Based Sustainable and High-Voltage Aqueous Flow Battery. *Energy Storage Mater.* **2019**, *19*, 62−68.

(42) Liu, B.; Tang, C. W.; Jiang, H.; Jia, G.; Zhao, T. An Aqueous Organic Redox Flow Battery Employing a Trifunctional Electroactive Compound as Anolyte, Catholyte and Supporting Electrolyte. *J. Power Sources* **2020**, *477*, 228985.

(43) Hu, S.; Li, T.; Huang, M.; Huang, J.; Li, W.; Wang, L.; Chen, Z.; Fu, Z.; Li, X.; Liang, Z. Phenylene-Bridged Bispyridinium with High Capacity and Stability for Aqueous Flow Batteries. *Adv. Mater.* **2021**, *33*, 2005839.

(44) Liu, Y.; Li, Y.; Zuo, P.; Chen, Q.; Tang, G.; Sun, P.; Yang, Z.; Xu, T. Screening Viologen Derivatives for Neutral Aqueous Organic Redox Flow Batteries. *ChemSusChem* **2020**, *13*, 2245−2249.

(45) Luo, J.; Wu, W.; Debruler, C.; Hu, B.; Hu, M.; Liu, T. L. A 1.51 V pH Neutral Redox Flow Battery towards Scalable Energy Storage. *J. Mater. Chem. A* **2019**, *7*, 9130−9136.

(46) Hu, B.; Tang, Y.; Luo, J.; Grove, G.; Guo, Y.; Liu, T. L. Improved Radical Stability of Viologen Anolytes in Aqueous Organic Redox Flow Batteries. *Chem. Commun.* **2018**, *54*, 6871−6874.

(47) Barnes, J. C.; Juríček, M.; Strutt, N. L.; Frasconi, M.; Sampath, S.; Giesener, M. A.; McGrier, P. L.; Bruns, C. J.; Stern, C. L.; Sarjeant, A. A.; Stoddart, J. F. ExBox: A Polycyclic Aromatic HydroCarbon Scavenger. *J. Am. Chem. Soc.* **2013**, *135*, 183−192.

(48) Sun, Q.-F.; Iwasa, J.; Ogawa, D.; Ishido, Y.; Sato, S.; Ozeki, T.; Sei, Y.; Yamaguchi, K.; Fujita, M. Self-Assembled $M_{24}L_{48}$ Polyhedra and Their Sharp Structural Switch upon Subtle Ligand Variation. *Science* **2010**, *328*, 1144−1147.

(49) Bird, C. L.; Kuhn, A. T. Electrochemistry of the Viologens. *Chem. Soc. Rev.* **1981**, *10*, 49−82.

(50) Takahashi, K.; Nihira, T.; Akiyama, K.; Ikegami, Y.; Fukuyo, E. Synthesis and Characterization of New Conjugation-Extended Viologens Involving a Central Aromatic Linking Group. *J. Electrochem. Soc., Chem. Commun.* **1992**, *8*, 620−622.

(51) Pan, M.; Vijayaraghavan, R.; Zhou, F.; Kar, M.; Li, H.; Wang, C.; MacFarlane, D. R. Enhanced CO_2 Uptake by Intramolecular Proton Transfer Reactions in Amino-Functionalized Pyridine-Based ILs. *Chem. Commun.* **2017**, *53*, 5950−5953.

(52) Zhao, E. W.; Liu, T.; Jónsson, E.; Lee, J.; Temprano, I.; Jethwa, R. B.; Wang, A.; Smith, H.; Carretero-González, J.; Song, Q.; Grey, C. P. In Situ NMR Metrology Reveals Reaction Mechanisms in Redox Flow Batteries. *Nature* **2020**, *579*, 224−228.

(53) Schlemmer, W.; Nothdurft, P.; Petzold, A.; Riess, G.; Frühwirt, P.; Schmallegger, M.; Gescheidt-Demner, G.; Fischer, R.; Freunberger, S. A.; Kern, W.; Spirk, S. 2-Methoxyhydroquinone from Vanillin for Aqueous Redox-Flow Batteries. *Angew. Chem., Int. Ed.* **2020**, *59*, 1−5.

(54) Wang, Y.; King, J. R.; Wu, P.; Pelzman, D. L.; Beratan, D. N.; Toone, E. J. Enthalpic Signature of Methonium Desolvation Revealed in a Synthetic Host−Guest System Based on Cucurbit[7]uril. *J. Am. Chem. Soc.* **2013**, *135*, 6084−6091.

(55) Roy, I.; Bobbala, S.; Zhou, J.; Nguyen, M. T.; Nalluri, S. K. M.; Wu, Y.; Ferris, D. P.; Scott, E. A.; Wasielewski, M. R.; Stoddart, J. F. ExTzBox: A Glowing Cyclophane for Live-Cell Imaging. *J. Am. Chem. Soc.* **2018**, *140*, 7206−7212.